

Bilayer graphene phonovoltaic-FET: *In situ* phonon recycling

Corey Melnick* and Massoud Kaviani

Department of Mechanical Engineering, Ann Arbor, University of Michigan, Michigan 48105-2125, USA

(Received 28 July 2017; revised manuscript received 18 October 2017; published 29 November 2017)

A new heat harvester, the phonovoltaic (pV) cell, was recently proposed. The device converts optical phonons into power before they become heat. Due to the low entropy of a typical hot optical phonon population, the phonovoltaic can operate at high fractions of the Carnot limit and harvest heat more efficiently than conventional heat harvesting technologies such as the thermoelectric generator. Previously, the optical phonon source was presumed to produce optical phonons with a single polarization and momentum. Here, we examine a realistic optical phonon source in a potential pV application and the effects this has on pV operation. Supplementing this work is our investigation of bilayer graphene as a new pV material. Our *ab initio* calculations show that bilayer graphene has a figure of merit exceeding 0.9, well above previously investigated materials. This allows a room-temperature pV to recycle 65% of a highly nonequilibrium, minimum entropy population of phonons. However, full-band Monte Carlo simulations of the electron and phonon dynamics in a bilayer graphene field-effect transistor (FET) show that the optical phonons emitted by field-accelerated electrons can only be recycled *in situ* with an efficiency of 50%, and this efficiency falls as the field strength grows. Still, an appropriately designed FET-pV can recycle the phonons produced therein *in situ* with a much higher efficiency than a thermoelectric generator can harvest heat produced by a FET *ex situ*.

DOI: [10.1103/PhysRevB.96.205444](https://doi.org/10.1103/PhysRevB.96.205444)**I. INTRODUCTION**

When energy is released in a device, it typically excites the electronic system. The resulting nonequilibrium (hot) electrons relax by colliding with the crystal lattice and releasing a narrow spectrum of optical phonons. Then, this nonequilibrium (hot) population of optical phonons thermalize by down-converting into multiple low-frequency acoustic phonons. The resulting, broad spectrum of acoustic phonons is the primary component of heat, and it has substantially more entropy than its precursor: the narrow spectrum of nonequilibrium optical phonons. Therefore, intervening before the hot optical phonon population thermalizes and harvesting it should enable a substantially higher conversion efficiency than that achieved in conventional heat harvesters such as the thermoelectric (TE) generator. However, the thermalization process typically occurs on the picosecond and nanometer scales, the maximum optical phonon energy is less than 500 meV, and typical optical phonon energies are below 75 meV [1–3]. In combination, these factors make targeting and harvesting a hot optical phonon population very challenging. Indeed, most attempts have predicted limited success [4–7]. The recently proposed phonovoltaic (pV) cell is an exception. Indeed, the device can theoretically utilize the low entropy of nonequilibrium optical phonon populations in order to approach the Carnot limit [8–10].

The phonovoltaic cell harvests optical phonons much like a photovoltaic harvests photons [8]. That is, a nonequilibrium (hot) population of optical phonons more energetic than the electronic band gap ($E_{p,o} > \Delta E_{e,g}$) relaxes by generating electron-hole pairs in a diode (e.g., a *pn* junction), which splits them to produce power. There are a few major obstacles which inhibit its successful operation. First, only a few

semiconductors have an optical phonon mode more energetic than their electronic band gap [10]. Second, only a few semiconductors have an optical phonon mode substantially more energetic than 26 meV (the thermal energy at room temperature). Assuming the band gap of these materials could be tuned to their optical phonon energy, a diode would not work at room temperature and thermally excited carriers would inhibit phonon-induced generation. Finally, optical phonon populations relax not only by generating electrons, but also by scattering with defects, isotopes, or by down-converting into multiple, low-energy acoustic modes. These alternate relaxation pathways produce heat rather than power and reduce the quantum efficiency of a phonovoltaic cell [8].

Graphene is perhaps the only material which can succeed in a phonovoltaic [10]. It has extremely energetic optical phonon modes (198 and 164 meV) [11,12] which primarily scatter with electrons, rather than other phonon modes [13,14]. Additionally, a band gap can be opened and tuned in the semimetal, such that its band gap approaches the optical phonon energy. This can be done through its chemical functionalization [15,16] or doping [17], through its deposition on an ordered substrate [18], or through the application of magnetic [19] or electric fields [20–22] (as shown in Fig. 1). No other material has been shown to be viable, although it is possible that organic macromolecules could be tuned to succeed, as they also exhibit extremely energetic vibrations, and those within the backbone chains could theoretically interact quickly with electrons in the LUMO and HOMO. However, our focus remains on the tuned graphene materials, as the highest reported phonovoltaic figure of merit in a tuned graphene material remains at a modest 0.6 (graphene:BN [10]), as much of the important groundwork is done, and as graphene-based devices are attractive targets for phonovoltaic incorporation.

Indeed, incorporating a phonovoltaic into a bilayer graphene field-effect transistor (FET) to create a FET-pV (as shown in Fig. 1) is a reasonable goal: the FET is a nanoscale

*cmelni@umich.edu

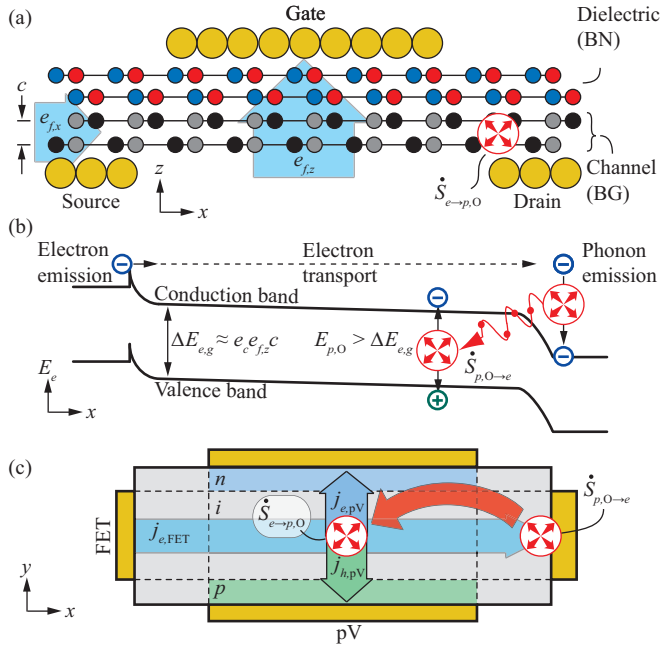


FIG. 1. (a) Atomic (b) and energetic illustrations of a bilayer graphene FET. A cross-plane field ($e_{f,z}$) applied to bilayer graphene opens a band gap ($\Delta E_{e,g}$) comparable to the potential induced between the two graphene layers ($e_e e_{f,z} c$, where e_e is the electron charge and c is the distance between graphene layers). This band gap impedes the transport of electrons from source to drain. Those electrons which are emitted from the source flow across the channel and emit optical phonons near the drain. (c) If the gate voltage is tuned such that the optical phonon energy ($E_{p,o}$) is greater than the band gap, these optical phonons can be recycled in an *in situ* phonovoltaic, which harvests optical phonons much like a photovoltaic harvests photons.

device which produces a large amount of heat, the mitigation of which remains crucial in the continued campaign to shrink transistor size and increase switching frequencies [21]. Moreover, experimental results show that bilayer-graphene FETs can exhibit a narrow band gap in the range of interest [23–25]. Theoretical calculations support this result and predict that the electronic density of states drastically increases near the band edge under high fields [26–28]. This should greatly increase the interband electron-phonon scattering rate. Indeed, our density functional and tight-binding theory calculations show that the interband electron-phonon scattering rate in bilayer graphene increases substantially at high fields. This phenomenon allows bilayer graphene to reach a record phonovoltaic figure of merit (0.9) and enable a phonovoltaic efficiency above 65%.

However, the phonovoltaic figures of merit reported above and in previous papers [9,10] assume that the hot optical phonon population is contained within a single point in k_p space. That is, they are evaluated for the Γ -point E_{2g} optical phonon mode. In a FET, the strong in-plane field will induce a hot optical phonon population with substantially more entropy. This entropy, i.e., the spread of momenta across which the optical phonon modes are heated, could reduce the figure of merit substantially. Thus, we perform full-band Monte Carlo simulations of the electron and phonon dynamics in bilayer graphene under strong in-plane and cross-plane electric fields

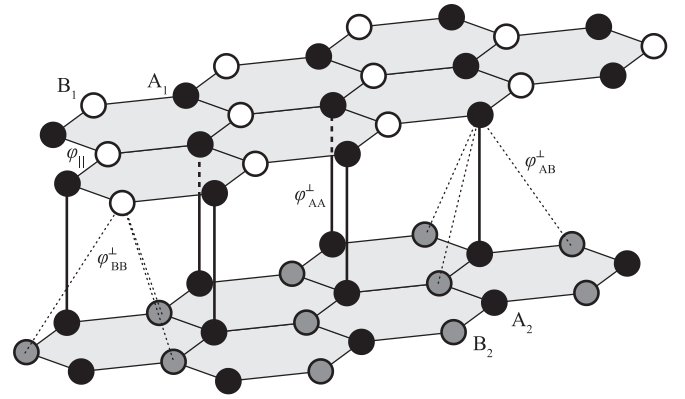


FIG. 2. The AB-stacked bilayer graphene lattice and its nearest-neighbor hopping interactions within the tight-binding model: in-plane hopping parameter $\phi_{||}$ and cross-plane parameters ϕ_{ij}^{\perp} [34].

to explore this topic. These simulations support our hypothesis, indicating that phonovoltaic performance suffers under strong fields. However, when the potential between the source and drain is close to the optical phonon energy, the figure of merit remains substantial. Indeed, our simulations suggest that the optical phonons produced in a FET-pV could be recycled with up to 50% efficiency. This is a drastic improvement over a typical *ex situ* heat recovery device such as the TE generator. Moreover, it is a drastic improvement over previously proposed *in situ* phonon harvesters, e.g., graded heterobarriers in a channel which recycle optical phonons with, at best, 20% efficiency [6,7].

II. BILAYER GRAPHENE

Let us begin our investigation by discussing the material in question, bilayer graphene. The hexagonal lattice of graphene can be divided into three triangular sublattices (A, B, and C). The first two contain one carbon atom per unit cell and the third defines the vacant centers of the carbon rings. Bilayer graphene is created by stacking two layers of graphene in the AA, AB, or twisted configurations. In AA-stacked graphene, the sublattices of both graphene layers are aligned. In AB-stacked graphene, only the A sublattices are aligned, while the B sublattices are aligned with the vacant sublattice C of the neighboring graphene layer, as shown in Fig. 2. In twisted bilayer graphene, one layer of graphene is twisted with respect to the other by some angle between 0° (AA stacking) and 60° (AB stacking) [25,29]. This twisting creates a Moiré pattern with local AA- and AB-like domains [28,30,31]. While the AB-stacked configuration is the most stable, the other stacking configurations are sufficiently close in energy that creating a perfectly AB-stacked bilayer graphene remains difficult and small twisting angles are often observed in experiments [32,33].

A. Electronic properties

In bilayer graphene, as in graphene and graphite, the time-reversal symmetry and sp^2 hybridization of the crystal leads to degenerate valence and conduction bands at the K and K' points of the Brillouin zone (BZ) [29,31,34–36]. In graphene

and AA bilayer graphene, these degenerate bands have no dispersion, such that their electrons behave like massless Dirac fermions and the K and K' wave vectors are named the Dirac points [34]. In AB-stacked bilayer graphene, the difference in the interlayer interactions between A and B site carbons (e.g., the tight-binding hopping interactions φ_{AA}^\perp , φ_{AB}^\perp , and φ_{BB}^\perp , as shown in Fig. 2 and discussed in Appendix A) adds mass to the valence and conduction bands near the K points [34]. Still, these points are commonly referred to as the Dirac points. In twisted bilayer graphene, some degeneracy remains at most twist angles, although it has been predicted that a substantial band gap forms for specific Moiré lattices (e.g., for twist angle 21.7°) and a more complex Fermi surface forms in twisted bilayer graphene with small twist angles under a field [28].

When an electric field is applied to bilayer graphene, it drives electrons from one layer into the other. In AB-stacked graphene, the electrons prefer to accumulate near the A sublattice sites due to their stronger interlayer interactions. This breaks the time-reversal symmetry of the crystal and thus opens a band gap at the (former) Dirac points [34,37]. In contrast, the interlayer interactions between both sublattices are identical in AA-stacked graphene. Thus, the electric field does not break the time-reversal symmetry, and it does not open a band gap. Instead, it splits the doubly degenerate bands around the Dirac points [36]. These effects and their causes are well modeled by a simple tight-binding (TB) model, as shown in Appendix A. In contrast, the electronic response of twisted-bilayer graphene is less well established. Indeed, it is not immediately clear how the local AA-like and AB-like domains in twisted bilayer graphene will respond to an applied electric field. However, experiments show that an applied electric field can open a band gap [25], and a recent study shows that this tunable band gap is due to excitonic effects which arise in small twist angle configurations of bilayer graphene but not in the large angle variants [31].

The ability to open and tune a band gap is central to the success of a phonovoltaic material [10]. Indeed, the band gap must be tuned to some energy near to but less than the optical phonon energy [8]. Thus, AB-stacked and small angle twisted bilayer graphene are attractive candidates. Here, we focus primarily on AB-stacked graphene, as computational limits preclude the simulation of small angle twisted bilayer graphene within density functional theory (DFT) and density functional perturbation theory (DFPT). Indeed, when we refer to bilayer graphene in the following sections, we are referring to AB-stacked bilayer graphene unless we explicitly specify a different stacking configuration. However, we will still present tight-binding results for twisted bilayer graphene which suggest that it works well as a phonovoltaic material. Let us overview our DFT and DFPT methodology before discussing the quantitative features of bilayer graphene.

The DFT and DFPT simulations are carried out using QUANTUM ESPRESSO [38] under the local density approximation and with norm-conserving pseudopotentials [39] on a fine $120 \times 120 k_e$ mesh. (The fine mesh density is required to capture the small details of the distorted bands near the K and K' points.) 15 \AA of vacuum is left between periodic images of the bilayer graphene, and a lattice constant (a) of 2.42 \AA with an interlayer spacing (c) of 3.35 \AA is used. The interlayer potential is prescribed by applying a saw-toothed electric

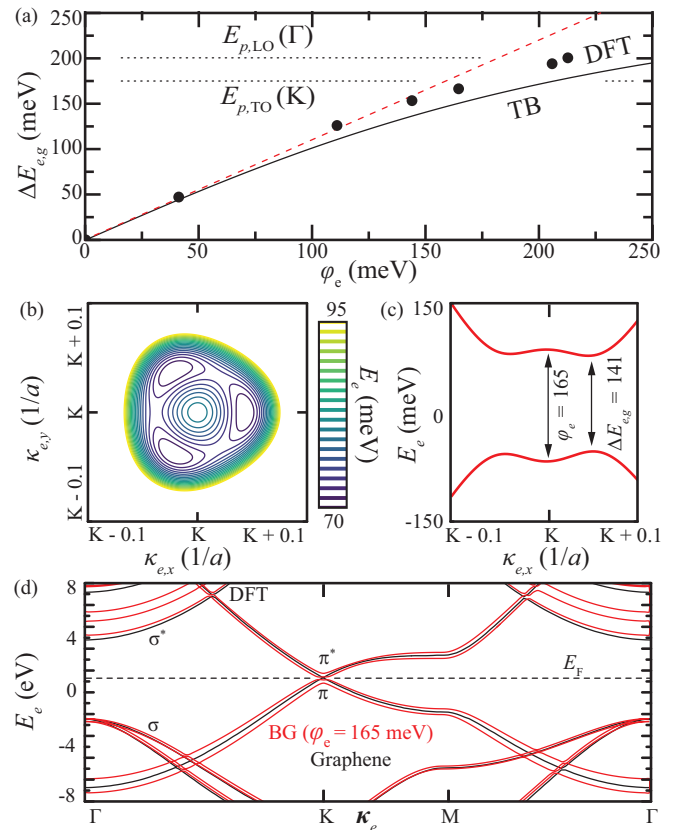


FIG. 3. (a) The band gap as a function of the cross-plane potential within DFT and the TB model, (b) low-energy equienergy lines for the first-conduction band, (c) low-energy band structure in bilayer graphene, and (d) the full band structure of graphene and bilayer graphene under a field. In the low-potential regime, the band gap equals the potential. As the potential increases, the low-energy surface becomes “hat”-like, as shown in (b) and (c), and the band gap grows more slowly than the applied cross-plane potential does.

potential in the cross-plane direction and placing the bilayer graphene within the monotonic portion of this potential. Thus, the interlayer potential equals the electric field strength times the interlayer spacing. Now, let us move on to a discussion of our results.

As shown in Fig. 3(a), the band gap in AB-stacked bilayer graphene is proportional to the electric potential between the two graphene layers, φ_e . Indeed, TB models show that the band gap equals the electric potential when it is below 50 meV. DFT tends to underestimate the band gap by $\frac{1}{3}$, so we scale the electric field by 3 to recover this trend. The divergence from this scaling is caused by the distortion of the π bands near the K points at higher fields. Indeed, while the energy gap between the π bands at the Dirac points continues to equal φ_e , the conduction (valence) band dips (rises) along the three K-M lines and the low-energy surface begins to resemble a trifold hat, as shown in Figs. 3(b) and 3(c). Outside of this small region, the graphene and bilayer graphene band structures are very similar, even under moderate fields, as shown in Fig. 3(d).

These electronic properties are well established [34,37]. As discussed above, they are the result of the discrepancy in

interlayer interactions in AB-stacked bilayer graphene and the loss of the time-reversal symmetry upon imposing a cross-plane electric field. Less well established are the effects these electronic changes have on the electron-phonon coupling. In the following section, we will calculate the electron-phonon coupling and the resulting electron-phonon scattering rate.

B. Electron-phonon scattering rate

An electron in state $|\mathbf{k}_e, i\rangle$ (wave vector \mathbf{k}_e and band i) can be scattered to state $|\mathbf{k}'_e, j\rangle$ by a phonon with momentum $\mathbf{k}_p = \mathbf{k}'_e - \mathbf{k}_e$ and polarization α due to the electron-phonon coupling given by matrix element $M_{e-p}^{(ij,\alpha)}(\mathbf{k}_e, \mathbf{k}_p)$, as discussed in Appendix B. Here, we evaluate the differential electron-phonon scattering rate $\dot{\gamma}_{e-p}^{(ij,\alpha)}(\mathbf{k}_e, \mathbf{k}_p)$, using the Fermi golden rule. That is,

$$\dot{\gamma}_{e-p}^{(ij,\alpha)}(\mathbf{k}_e, \mathbf{k}_p) = \frac{2\pi}{\hbar} |M_{e-p}^{(ij,\alpha)}(\mathbf{k}_e, \mathbf{k}_p)|^2 \times \delta(E_{\mathbf{k}_e, i} - E_{\mathbf{k}_e + \mathbf{k}_p, j} \pm \hbar\omega_{\mathbf{k}_p, \alpha}) \Omega, \quad (1)$$

where Ω accounts for the relevant population factors. Thus, to calculate the rate at which a particular phonon mode scatters with all electron states, $\dot{\gamma}_{e-p}^{(ij,\alpha)}(\mathbf{k}_p)$, the differential rate is summed across all electron wave vectors and bands, and $\Omega \simeq f_e - f'_e$, where f_e and f'_e are the occupancies of the initial and final electron states. In this case, Ω prevents intraband events from contributing substantially to the phonon lifetime unless the Fermi level lies within a few $k_B T$ of the valence or conduction bands [10]. Indeed, in a nondegenerate semiconductor, $\Omega \simeq 1$ for transitions from the valence to conduction bands and $\Omega \simeq 0$ otherwise. Under this condition,

$$\dot{\gamma}_{e-p}^{(ij,\alpha)}(\mathbf{k}_p) \simeq \dot{\gamma}_{e-p}^{(cv,\alpha)}(\mathbf{k}_p) = \sum_{\mathbf{k}_e} \frac{2\pi}{\hbar} |M_{e-p}^{(cv,\alpha)}(\mathbf{k}_e, \mathbf{k}_p)|^2 \times \delta(E_{\mathbf{k}_e, v} - E_{\mathbf{k}_e + \mathbf{k}_p, c} \pm \hbar\omega_{\mathbf{k}_p, \alpha}), \quad (2)$$

where $i = v$ is the valence band and $j = c$ is the conduction band.

Here, this integration is carried out for the E_{2g} and A'_1 modes using DFT/DFPT and using the TB model. A Lorentzian δ function with 2 meV of smearing is used to achieve convergence on a 500×500 \mathbf{k}_e mesh (using interpolation for the DFT calculations). Figure 4 shows the results. The TB theory and DFT/DFPT simulations show strong agreement at low fields, as shown in Fig. 4(b), but not at high fields. In both, the interband electron-phonon scattering rate remains stable as the band gap increases, until the band gap approaches the optical phonon energy, at which point scattering increases drastically. This trend stands in stark contrast with that predicted for other tuned graphene materials, e.g., graphene:BN, where the scattering rate vanishes as the band gap approaches the optical phonon energy [10]. This beneficial phenomenon is a result of the transition from a quadratic dispersion to the hatlike low-energy surface in bilayer graphene under high fields. In a typical material with a parabolic low-energy surface, the density of electronic states vanishes at the band edge. Thus, the number of energy-conserving transitions vanishes as the band gap approaches the optical phonon energy. However, the hatlike band structure of bilayer graphene creates a large

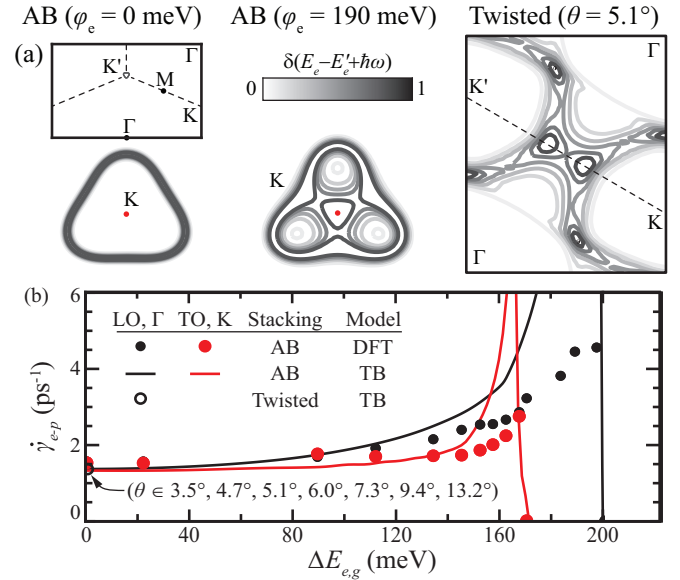


FIG. 4. (a) Energy-conserving δ function for the E_{2g} mode in bilayer graphene, (b) the interband electron-phonon scattering rates for an x -polarized E_{2g} mode. The scattering rate increases drastically as $\varphi_e \approx E_{p,0}$ and peaks around $\Delta E_{e,g} \approx E_{p,0}$ due to the increase in the number of electronic states which participate in interband electron-phonon scattering.

density of electronic states near the band edge, such that the number of energy-conserving transitions is maximized when $\Delta E_{e,g} \simeq E_{p,0}$, as shown in Fig. 4(a).

Despite the agreement between the DFT and TB results for bilayer graphene under weak and moderate-strength fields, the TB theory predicts much faster scattering than DFT does for bilayer graphene under a strong field. This discrepancy is explained here by the simplicity of the TB theory, which does not take into account many features of the electron Hamiltonian, e.g., the electron-electron repulsion, which become important as the field drives multiple electrons into each atomic orbital of the charged graphene layer. Thus, we would prefer to use DFT results. Indeed, we use them unless otherwise specified. However, the large number of atoms in a twisted bilayer graphene unit cell preclude its simulation within DFT and DFPT, particularly for smaller twisting angles. Thus, we must rely on our TB model to calculate the electron-phonon coupling for the twisted stacking configuration. Even within the TB model, evaluating the electron-phonon scattering rate becomes unreasonable for very small twisting angles, and the TB model does not predict the formation of a band gap in twisted bilayer graphene when it is subjected to a cross-plane field. Thus, our ability to predict the phonovoltaic performance of twisted bilayer graphene is limited to the no-field and moderate twist angle cases. We further limit our investigation to the less computationally intensive E_{2g} mode. Within this limited scope, our results show that the electron-phonon scattering rate remains unaffected by the twisting angle, as shown in Fig. 4. Let us examine this result.

First, we note that the electron-phonon scattering rate is dominated by the nearest-neighbor in-plane interactions, as discussed in Appendix A. That is, it is dominated by the

interaction between the valence electrons in the atomic orbitals of one sublattice and conduction electrons in the atomic orbitals of the second sublattice. Thus, as long as the stacking order (or electric field) does not separate the conduction and valence wave functions in space by more than the sublattice, the perturbation will not affect the electron-phonon matrix elements. Our TB model shows that the electric field drives the conduction and valence electrons into a specific layer, and the twisting angle tends to drive the conduction and valence electrons into the AA-like domain (as previously shown [30]). In either case, the valence and conduction wave functions are at most separated by the sublattice, rather than, e.g., the layer or the domain. Thus, the electron-phonon coupling matrix elements remain negligibly affected by the electric field or the twisting angle.

Second, we note that the electronic density of states available for scattering is negligibly affected by the twisting angle. Indeed, while the energy-conserving contours become more complex as the twisting angle falls below 5° , as shown in Fig. 4 the complexity is not created by a fundamental deformation of the band structure (as in bilayer graphene subjected to a cross-plane field). Instead, it is primarily created by the folding of the graphenelike dispersion into the BZ of the twisted bilayer graphene. That is, as the twisting angle decreases, the twisted bilayer graphene unit cell contains an increasing number of graphene unit cells, and the twisted bilayer graphene BZ folds in more wave numbers of the graphene BZ. Eventually, the separate Dirac cones of graphene overlap within the very small BZ of twisted bilayer graphene and create more complex low-energy surfaces. At sufficiently small twisting angles, quasibound states in the AA-like domains form [30]. However, there is no evidence that this affects $\dot{\gamma}_{e-p}^{(E_{2g})}$. Indeed, the insensitivity of $\dot{\gamma}_{e-p}^{(E_{2g})}$ to the twisting angle is supported by experimental Raman studies [40,41]. Interestingly, these studies also show that the linewidth of the A'_1 mode increases as the twisting angle approaches either a critical angle of 10° or 0° . Moreover, they showed that this is caused by the formation of a Van Hove singularity [41]. While the A'_1 mode can interact with this singularity, the E_{2g} mode cannot. Indeed, the E_{2g} electron-phonon coupling element vanishes near the M point (where this singularity forms) due to the crystal symmetries.

Regardless, the electron-phonon scattering rate is either maintained or enhanced in small angle twisted bilayer graphene. As its band gap can be tuned by the application of a cross-plane field [25,31], it should serve as a suitable phonovoltaic material. However, quantifying its phonovoltaic performance is outside the scope of this study. Here, the main thrust is to examine the hot optical phonons produced by a realistic optical phonon source and to determine the effect the resulting nonequilibrium phonon population has on phonovoltaic operation. Restricting our investigation to AB-stacked graphene allows us to pursue this investigation without requiring a massive computational effort. Moreover, it simplifies the results so that we can extract more instructive conclusions. Thus, a detailed analysis of twisted bilayer graphene as a phonovoltaic material is left for future study. However, we do need to determine the phonovoltaic performance of bilayer graphene in order to quantify how significantly

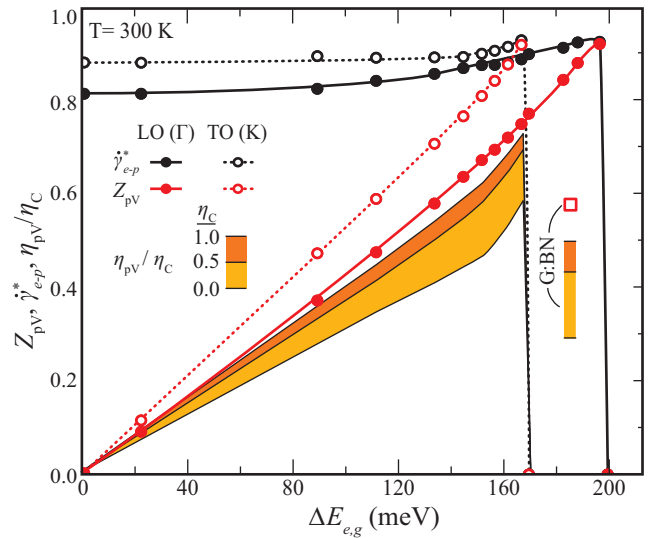


FIG. 5. The phonovoltaic performance metrics: the figure of merit Z_{pV} , quantum efficiency $\dot{\gamma}_{e-p}^*$, and efficiency η_{pV} . Due to the increase in the interband electron-phonon scattering rate as the band gap approaches the optical phonon energy, the figure of merit exceeds 0.9 for both phonon modes, enabling an efficiency exceeding 65% of the Carnot efficiency, even at 300 K. Graphene:BN results are added for comparison [10].

the entropy in the phonon population degrades phonovoltaic performance. Let us proceed with this calculation.

C. Phonovoltaic performance

From Phonovoltaic I [8], the phonovoltaic performance is primarily determined by the Carnot limit (η_C) and material figure of merit (Z_{pV}), which encapsulates the fraction of the optical phonon energy preserved by the band gap and the fraction of the optical phonons which generate electrons rather than heat ($\dot{\gamma}_{e-p}^*$), or

$$Z_{pV} = \frac{\Delta E_{e,g}}{E_{p,O}} \dot{\gamma}_{e-p}^* \simeq \frac{\Delta E_{e,g}}{E_{p,O}} \frac{\dot{\gamma}_{e-p}}{\dot{\gamma}_{p-p} + \dot{\gamma}_{e-p}}. \quad (3)$$

Then, the efficiency is

$$\eta_{pV} \simeq \eta_C Z_{pV} F_F^*, \quad (4)$$

where F_F^* is the adjusted fill factor, calculated using a simple diode and heat equation, as in Phonovoltaic I [8].

Figure 5 presents the phonovoltaic performance metrics for bilayer graphene. Here, we assume that the phonon-phonon lifetime in bilayer-graphene is identical to that in graphene and independent of the cross-plane electric field. This is reasonable, as the phonon lifetime in bilayer graphene is the same as that in graphene [13,42,43], and the in-plane force constants which determine the phonon properties are dominated by the σ bonds, which themselves are nearly unaffected by asymmetry [10]. As shown, the figure of merit reaches a record 0.9, a substantial improvement on the record Z_{pV} of 0.6 in graphene:BN [10]. The hatlike energy surfaces which lead to very fast electron-phonon scattering as $\Delta E_{e,g} \rightarrow E_{p,O}$ enable this large figure of merit. Moreover, it enables a “heat” harvesting efficiency of over 65% of the

Carnot limit, triple that of a typical thermoelectric efficiency and comparable to or even in excess of the efficiency of a conventional power plant. While the electron-phonon coupling broadens the phonon energy and thus degrades the figure of merit and efficiency, the linewidth ($\Gamma_{ep} = \dot{\gamma}_{e-p}/\hbar$) is less than 2 meV for the A'_1 mode and 3.5 meV for the E_{2g} mode. Thus, we expect that these phenomena will impact the efficiency negligibly. However, it remains unclear how best to incorporate the phonovoltaic into a device, and it remains unclear how a real source of optical phonons would affect phonovoltaic performance. In the following sections, we investigate both of these topics through the Monte Carlo simulation of bilayer graphene under strong in-plane and cross-plane fields.

III. ELECTRON AND PHONON DYNAMICS UNDER STRONG FIELDS

Consider a bilayer graphene field-effect transistor (FET). A voltage between the FET source and drain creates an in-plane field in the FET channel which drives electrons from the source to the drain (see Fig. 1). When a gate (cross-plane) voltage is applied, a band gap forms, cutting off the flow of electrons from the source to the drain. If the gate voltage grows larger, a surface charge accumulates on the top graphene layer, such that the Fermi level moves into the bilayer graphene conduction bands and the semiconductor behaves like a metal, transporting electrons easily from the source to the drain. As long as electrons are flowing, a large number of optical phonons will be produced in the drain as the hot electrons scatter against the lattice. Monte Carlo simulations of nonequilibria in graphene under a strong in-plane field, for example, show that the optical phonon population can reach thousands of Kelvin [44]. In the phonovoltaic, that indicates a Carnot limit approaching unity. If a phonovoltaic can be embedded into the FET and recycle these phonons *in situ*, the heat production and power demands of the FET would be greatly reduced.

However, major obstacles present themselves. Of primary concern is the ability of the optical phonons generated by an electric field to drive the operation of a phonovoltaic. Note that optical phonons with wave vectors far from the Γ or K points are incapable of generating electrons, as shown in Fig. 6. Moreover, we can see that the conduction and valence band structures must be at least “in line” for any optical phonons emitted by field-accelerated electrons to generate electrons. That is, we can say that the surface tangent of the low-energy conduction bands must intersect with the valence bands. This statement is exactly true when the bands are dispersionless, as in graphene. Furthermore, we can say that the more that the surface tangents intersect, the larger the area of \mathbf{k}_p space which can contribute to electron generation. Thus, bilayer graphene, with its wide, hatlike trough, should enable a wide spectrum of optical phonons to generate electrons. However, it remains important to understand what fraction of the hot optical phonon population created by an in-plane electric field can contribute to electron generation. That way, we can quantify the effective figure of merit of bilayer graphene. To do this, we perform full-band Monte Carlo simulations of the coupled electron and phonon dynamics in bilayer graphene under a field.

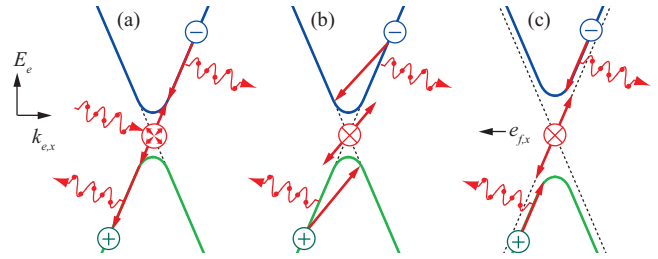


FIG. 6. The importance of band structure and phonon momentum in enabling phonovoltaic operation. (a) The valence and conduction bands are “in line”, such that optical phonons emitted as electrons fall down the steepest energy gradient can generate electrons. (b) However, optical phonons emitted during backscattering events can not generate electrons, as high-momentum phonons can not conserve energy and momentum in interband transitions. (c) If the valence conduction bands are not in line, then no optical phonons emitted in an intraband process can generate electrons, despite meeting the basic phonovoltaic criterion: $E_{p,0} > \Delta E_{e,g}$.

A. Monte Carlo simulations

The ensemble Monte Carlo (EMC) simulations track the evolution of the electron and phonon populations in bilayer graphene upon excitation of the electron population by an in-plane electric field. They do so by modeling of the electron and phonon Boltzmann transport equations (BTE) statistically. Here, we consider electron and phonon populations that do not vary in space, but do vary in momentum space (2D), such that the electron BTE is

$$\frac{\partial f_e(\mathbf{k}_e)}{\partial t} + \mathbf{e}_f \cdot \nabla_{\mathbf{k}_e} f(\mathbf{k}_e) = \left. \frac{\partial f_e(\mathbf{k}_e)}{\partial t} \right|_s, \quad (5)$$

where \mathbf{e}_f is the electric field and $\partial f_e(\mathbf{k}_e)/\partial t|_s$ represents the net scattering of electrons into wave vector \mathbf{k}_e . Here, scattering with the LO and TO phonon modes at the Γ and K points, respectively, is considered and a rejection technique is used to capture the effects of degeneracy. The low-energy electron bands and electron-phonon coupling elements are calculated using the tight-binding model presented in Appendix A, but fit to the DFT results, and the phononic dispersion is calculated within DFPT. In-between these scattering events, the electrons are accelerated by a constant electric field ($\mathbf{e}_f = e_{f,x}$). The electron ensemble (5×10^6 superparticles) is simulated in time steps of 0.1 ps, during which time the number of optical phonons emitted in each \mathbf{k}_p bin is counted, and after which the phonon occupation is updated according to the phonon BTE:

$$\frac{\partial f_p(\mathbf{k}_p)}{\partial t} = \dot{S}(\mathbf{k}_p) - \frac{f_p(\mathbf{k}_p) - f_p^\circ(\mathbf{k}_p)}{\tau_{pp}}, \quad (6)$$

where \dot{S} is the net source of optical phonons due to intraband electron-phonon scattering events, f_p is the phonon occupancy, f_p° is the equilibrium phonon occupancy, and τ_p is the phonon lifetime. Then, the integrated and differential scattering rates are updated for the next time step of the EMC electron simulation. In this manner, the electron and phonon nonequilibria in bilayer graphene are tracked after a strong in-plane electric field is applied.

Before moving on to the evaluation of the phonovoltaic performance, two simulations are performed in order to

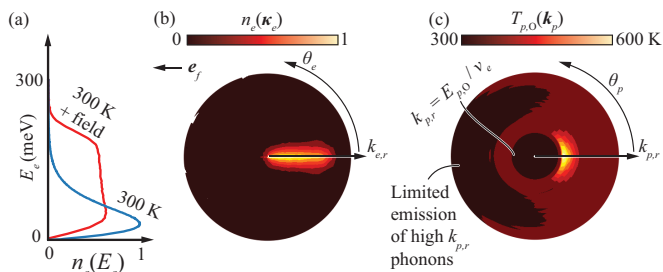


FIG. 7. (a) The normalized electronic energy and (b) momentum distribution, and (c) the phonon (TO) momentum distribution in a “toy” nondegenerate graphene with dispersionless bands under a strong in-plane electric field. The electron particles are accelerated by the field, creating an electron stream in the opposite direction. Once they reach kinetic energy $\epsilon_{k_e} = E_{p,0}$, they can emit an optical phonon and return to one of the conduction band valleys at K or K' and fall to the bottom of the stream. These phonon emission events all happen in a narrow area of \mathbf{k}_e space, such that only there is only a small area in \mathbf{k}_p space which conserve energy and momentum, and only this small area is heated.

qualitatively describe what happens to the electron and phonon populations and to validate the simulations. The first simulation uses the full detail of the electric bands from tight-binding theory. The second uses a “toy” tuned-graphene material, i.e., one with a radially symmetric and dispersionless band structure at the K and K' points with $E_e = \hbar v_e |\mathbf{k}_e|$, where v_e is the constant electron speed. (In the TB model of graphene, $v_e = 2a_o \varphi_{\parallel} / 3\hbar$, where a_o is the interatomic distance and φ_{\parallel} is the intralayer hopping strength.) The latter is used to illustrate the fundamental behavior of an electron population under a strong field, and the former is used to investigate how the unique low-energy structure of bilayer graphene affects the resulting nonequilibria. The initial and steady-state results are presented in Figs. 7 and 8.

Let us discuss the “toy” graphene results first. Initially, the electron population has a typical energy distribution $n_e(E_e) \simeq D_e f_e^o$, where D_e is the electronic density of states and f_e^o is

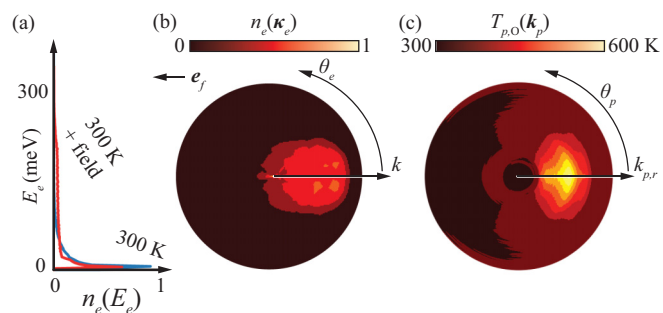


FIG. 8. (a) The normalized electronic energy and (b) momentum distribution, and (c) the phonon (TO) momentum distribution in full-band bilayer graphene under a 165-meV cross-plane electron potential and a strong in-plane electric field. Qualitatively, the electron and phonon behavior resemble those in the dispersionless graphenelike material (Fig. 7). However, the broad valley in the hatlike low-energy surface broadens the momentum distribution of both the electron stream and the phonons produced by its relaxation.

the Fermi-Dirac distribution. Then, a strong in-plane field is applied. This accelerates the electron population, increasing the $-\mathbf{e}_f$ momentum component of each electron and exciting the population. The electrons tend to stream along this $-\mathbf{e}_f$ vector until they have sufficient energy to emit a phonon. That is, they accelerate until their kinetic energy reaches the optical phonon energy (plus the Fermi energy), at which point they quickly emit a phonon and relax back to start of this stream, i.e., the band edge (Fermi level), where the parentheses denote a degenerate or nondegenerate semiconductor.

This behavior is well reported in the literature [44,45], providing some validation of our simulations. We note that scattering with the acoustic branches and other electron would distribute the electrons outside of this stream. The electron-electron interactions are important in a nondegenerate semiconductor while the the acoustic phonon interactions contribute in the low-field, nondegenerate case. While the stream width will increase the entropy of the coupled phonon system, it will primarily increase entropy in the phonon direction ($\mathbf{k}_{p,\theta}$), rather than the phonon magnitude ($\mathbf{k}_{p,r} = |\mathbf{k}_p|$). Thus, it will have little effect on the phonovoltaic figure of merit, and we can safely neglect these interactions which greatly increase the computational burden.

While the electron population is confined to a narrow stream in \mathbf{k}_e space, the hot optical phonon population created by this stream is even more confined, both in the direction of \mathbf{e}_f and perpendicular to it. This confinement is a result of the narrow electron stream and the small region of \mathbf{k}_e space wherein electrons emit optical phonons. Note that an intraband emission event can create optical phonons with, at minimum, a momentum of $\hbar |\mathbf{k}_p|_{\min} = E_{p,0} / v_e$, where we assume the Fermi level lies outside the conduction band of a nondegenerate semiconductor. This is the only region of \mathbf{k}_p space heated by electrons with kinetic energy $E_e = \hbar v_e |\mathbf{k}_e| = E_{p,0}$. While more energetic electrons can produce these minimum momentum optical phonons, they can also backscatter and produce optical phonons with more momentum. Precisely, they can produce phonons with a momentum between $E_{p,0} / v_e$ and $(2E_e - E_{p,0}) / v_e$. If we assume that the majority of electrons will emit an optical phonon within their lifetime ($1 / \dot{\gamma}_{e-p}$), electrons can exceed the optical phonon energy by $e_c |\mathbf{e}_f| v_e / \dot{\gamma}_{e-p}$ before emitting an optical phonon, and the region of \mathbf{k}_p space which is substantially heated will lie within $\hbar |\mathbf{k}_p| \in [E_{p,0} / v_e, E_{p,0} / v_e + e_c |\mathbf{e}_f| / \dot{\gamma}_{e-p}]$, with the hottest region near $\hbar |\mathbf{k}_p|_{\min}$. In a degenerate semiconductor, a wider range of \mathbf{k}_p space is heated. Consider a degenerate semiconductor at 0 K: in this case, the minimum energy required for phonon emission is not $E_{p,0}$, but $E_{p,0} + E_F$, where E_F is the Fermi energy relative to the band edge. Thus, the range of heated \mathbf{k}_p space is approximately $\hbar |\mathbf{k}_p| \in [(E_{p,0} + E_F) / v_e, (E_{p,0} + E_F) / v_e + e_c |\mathbf{e}_f| / \dot{\gamma}_{e-p}]$, and degenerate effects will generally reduce the phonovoltaic performance. In the following sections, we will focus on a nondegenerate semiconductor.

The full-band simulations of gated bilayer graphene under a strong in-plane and cross-plane electric field show similar trends. However, the electrons form a much wider stream, as the low-energy electron states are not contained in a narrow valley. Instead, they are contained in a broad, hatlike trough, and this enables optical phonon emission to a large ring of states, even when $E_e = E_{p,0}$. Thus, hot optical phonons

are created in a correspondingly broadened region of \mathbf{k}_p space. While this increase in entropy should inhibit phonovoltaic operation, the broad electronic trough allows many high-momentum optical phonons to participate in electron generation, and the optical phonon population still gains a high degree of nonequilibrium over time. In the following section, we quantify the effects this entropy has on phonovoltaic performance.

B. Phonovoltaic performance

Here, we calculate the total rate of generation and down-conversion which would occur for the given state of the phonon and electron populations after a steady state is reached in the MC simulations. (Note that no generation occurs within these simulations, as it is computationally impossible to simulate the electron, hole, and phonon populations with sufficient accuracy in both real and momentum spaces while accounting for drastic spatial variation in the electron and hole concentrations. In effect, we assume here that there is perfect and immediate extraction of generated carriers.) To calculate these quantities, we integrate the scattering rates over electron and phonon momentum spaces, i.e.,

$$\dot{\gamma}_{e-p}^{(cv,\alpha)} = \sum_{\mathbf{k}_e, \mathbf{k}_p} \dot{\gamma}_{e-p}^{(cv,\alpha)}(\mathbf{k}_e, \mathbf{k}_p) [f_p - f_e(\mathbf{k}_e) f_h(\mathbf{k}_e - \mathbf{k}_p)], \quad (7)$$

$$\dot{\gamma}_{p-p}^{(cv,\alpha)} = \sum_{\mathbf{k}_p} \dot{\gamma}_{p-p}^{(cv,\alpha)}(\mathbf{k}_p) (f_p - f_p^\circ), \quad (8)$$

where f_p and f_p° are the actual and equilibrium populations of the phonon mode with polarization α and wavevector \mathbf{k}_p and f_e and f_h are the populations of the electron and hole states involved in recombination. Then, the fraction of optical phonons which generate electrons rather than heat ($\dot{\gamma}_{e-p}^*$) is calculated, where we assume that down-conversion is the dominant mechanism driving heat generation. Dropping the (cv,α) superscripts, we have

$$\dot{\gamma}_{e-p}^* = \frac{\dot{\gamma}_{e-p}}{\dot{\gamma}_{e-p} + \dot{\gamma}_{p-p}}. \quad (9)$$

In the previous calculations of Z_{pV} , here and in the previous papers [9,10], we assumed a single point in phonon momentum space was heated. For example, we assumed that only the Γ point (E_{2g} mode) or the K point (A_1' mode) were driving phonovoltaic operation. We will call this the ideal $\dot{\gamma}_{e-p}^*$. Here, we account for the more realistic distribution of hot phonon modes near these two points in order to calculate the ‘‘real’’ $\dot{\gamma}_{e-p}^*$.

As shown in Fig. 9, the real $\dot{\gamma}_{e-p}^*$ can be substantially reduced from the ideal case. This trend is more pronounced under strong electric fields, where a larger region of \mathbf{k}_p space is heated, and when the band gap approaches the optical phonon energy, as a smaller region of \mathbf{k}_p space can participate in generation. Interestingly, the discrepancy between the ideal $\dot{\gamma}_{e-p}^*$ and real $\dot{\gamma}_{e-p}^*$ is not monotonic as the band gap increases. This, we hypothesize, is due to the transition from a parabolic to a hatlike band structure, which occurs around the same band gap as the $\dot{\gamma}_{e-p}^*$ recovery under moderate- or low-strength fields. That is, the region of \mathbf{k}_e space involved in generation increases as the hatlike surface forms, and this compensates

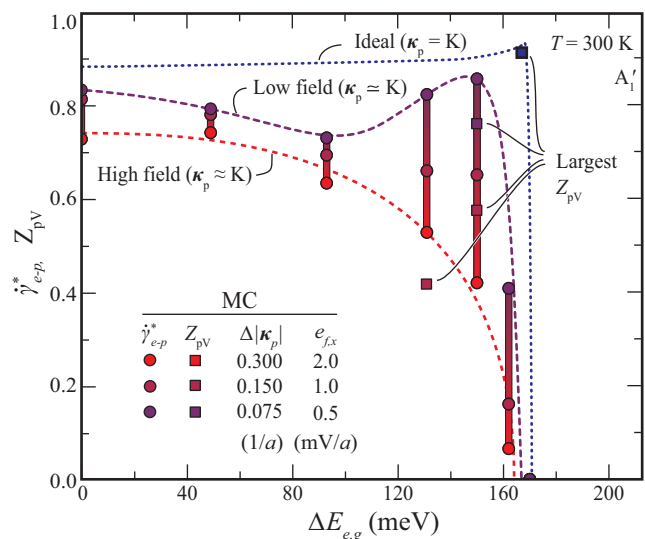


FIG. 9. $\dot{\gamma}_{e-p}^*$ of the A_1' phonon mode for variations in the band gap. These results are compared with the previously calculated (ideal) $\dot{\gamma}_{e-p}^*$ for variations in the applied electric field. At relatively low fields and small band gaps, there is good agreement, as the majority of hot optical phonons are contained within a narrow region of \mathbf{k}_p space ($\Delta|\mathbf{k}_p| \approx e_c e_{fx} / \hbar \dot{\gamma}_{e-p}$) and a substantial region of \mathbf{k}_p space is capable of contributing to electron generation. As the electric field strength grows and the band gap approaches the optical phonon energy, the optical phonons are produced in a larger region of \mathbf{k}_p space and the region of \mathbf{k}_p space that is capable of contributing to electron generation shrinks.

for the decrease in \mathbf{k}_p space, until very few intraband optical phonon emissions can actually contribute to generation. This compensation enables an *in situ* phonovoltaic to achieve an effective figure of merit above 0.75 under a weak field, which corresponds to an efficiency above 50% when there is a large degree of nonequilibrium (a Carnot limit approaching unity). In a realistic FET device, this weak-field condition could be effectively achieved by tuning the potential between source and drain: if this potential were close to but greater than the optical phonon energy, we can expect that the phonons emitted in the drain will be clustered in momentum space much like they are in the weak-field limit. Thus, we can expect the figure of merit to remain substantial, and we can expect the FET-pV to recycle 50% of the heat the FET produces.

IV. CONCLUSIONS

Here, we have evaluated the impact of a realistic phonon source on phonovoltaic operation. Previous phonovoltaic investigations assumed that the optical phonon source produced a nonequilibrium optical phonon population with the minimum entropy. That is, the nonequilibrium population is contained in a single mode E_{2g} and momentum $\mathbf{k}_p = \Gamma$. Here, we relax this assumption and investigate the entropy produced by a realistic optical phonon source and the effect this has on phonovoltaic performance. In doing so, we have explored a potential phonovoltaic application, the FET-pV. This investigation is primarily carried out using full-band MC simulations of the phonon and electron dynamics in a bilayer graphene FET.

To supplement this work, we use tight-binding simulations and DFT/DFPT calculations to characterize the electronic, phononic, and electron-phonon coupling properties of bilayer graphene under strong cross-plane fields.

We show that bilayer graphene can reach a pV figure of merit exceeding 0.9, largely due to the transition of its low-energy band structure from a classic parabolic shape to a highly nonparabolic, trifold-hat shape as a strong cross-plane electric field is applied. This band structure has a large, rather than vanishing, density of states near the band edge. Therefore, as the band gap approaches the optical phonon energy, the number of energy-conserving transitions increases drastically, the electron-phonon scattering rate increases substantially, and the phonovoltaic figure of merit approaches unity. With a highly nonequilibrium population of optical phonons contained at $\mathbf{k}_p = \text{K}$ or Γ (A_1 or E_{2g}), a bilayer graphene phonovoltaic can convert optical phonons into energy with an efficiency exceeding 65% at room temperature.

However, the full-band Monte Carlo simulations of the electron and phonon dynamics in a bilayer graphene FET show that a real phonon source substantially lowers this conversion efficiency, as high-momentum optical phonons are incapable of generating electrons. Indeed, the efficiency vanishes under a sufficiently strong in-plane electric field which accelerates electrons to very energetic states from where they can emit high-momentum phonons. Under a low-strength or well-tuned electric field, however, the momentum of optical phonons emitted by the excited electrons is relatively confined, and the phonovoltaic can harvest the resulting nonequilibrium population efficiently. Indeed, under weak fields, bilayer graphene exhibits an effective figure of merit around 0.75 and a bilayer graphene pV can harvest the nonequilibrium optical phonon population with an efficiency over 50%. Not only is this a drastic improvement over *ex situ* heat harvesters like the thermoelectric generator, but it is also a major improvement over previously proposed *in situ* phonon recycling devices [7].

While these results are promising, a major experimental effort is required to validate them. Primarily, it remains crucial to demonstrate the basic phonovoltaic principle: a phonovoltaic cell must be manufactured and then the phonovoltaic effect must be recorded. This effort is not trivial, as tuned graphene diodes remain difficult to manufacture, and as researchers must ensure any current or voltage measured is not, e.g., from a photocurrent rather than a phonocurrent. It is likely that the first experimental efforts will need to proceed at cryogenic temperatures and using a laser to excite the optical phonon modes, rather than a field. However, this study showcases that these efforts could one day lead to an impressive reduction in heat generation while simultaneously increasing the power budget in modern electronic packages.

ACKNOWLEDGMENTS

This work was supported by the NSF program on Thermal Transport and Processes (Award No. CBET1332807) and employed computing resources of the DOE National Energy Research Scientific Computing Center (Office of Science, Contract No. DE-AC02-05CH11231).

APPENDIX A: TIGHT-BINDING MODEL OF BILAYER GRAPHENE

The tight-binding model is built on the assumption that the electron wave functions can be built from a Bloch basis of atomic orbitals centered on each atom in the crystal. In graphene and its derivatives, only the $p_z(\mathbf{r} - \mathbf{R}_i)$ orbitals are required for an accurate prediction of the low-energy π bands, where $\mathbf{r} - \mathbf{R}_i$ is the position relative to the i th carbon atom [37]. Typically, the tight-binding Hamiltonian only considers the interaction between the atomic orbitals and the ionic potential of the atoms, V_i . This interaction is given by the integral $\varphi_{ij} = \langle p_z(\mathbf{r} - \mathbf{R}_i) | V_i | p_z(\mathbf{r} - \mathbf{R}_j) \rangle$. Here, we also consider the effects of the electric field, which creates a potential between the two graphene layers, φ_e . Thus, the Hamiltonian is

$$H = - \sum_{ij} \varphi_{ij} (d_i^\dagger d_j + \text{H.c.}) \pm \varphi_e d_i^\dagger d_j \delta_{ij}, \quad (\text{A1})$$

where d_i^\dagger and d_i are the creation and annihilation operators for an electron in the orbital centered on atom i , and the plus and minus signs correspond to the lower and upper layers, respectively. This Hamiltonian is invariant for translations along the lattice vectors \mathbf{A}_j , which allows us to Fourier transform the wave functions, their creation and annihilation operators, and the hopping interaction into \mathbf{k}_e space. The Fourier-transformed Hamiltonian becomes

$$H = \sum_{\mathbf{k}_e, nm} [\varphi_{nm, \mathbf{k}_e} d_{\mathbf{k}_e, n}^\dagger d_{\mathbf{k}_e, m} + \text{H.c.}], \quad (\text{A2})$$

where n and m are now restricted to atoms in the unit cell. Thus, the wave functions are built using a basis of N p_z orbitals, where N is the number of atoms in the unit cell. Upon Fourier transforming this basis into the vector $|\mathbf{k}_e\rangle$, we can rewrite our Hamiltonian as the $N \times N$ matrix with elements

$$H_{nm}(\mathbf{k}_e) = \langle \mathbf{k}_e, n | H | \mathbf{k}_e, m \rangle. \quad (\text{A3})$$

Assuming the basis is orthogonal, i.e., $\langle \mathbf{k}_e, n | \mathbf{k}_e, m \rangle = \delta_{n,m}$, the eigenvalues of this matrix give the eigenenergies of the electronic system at wave vector \mathbf{k}_e , and the eigenvectors describe the corresponding electron wave function. In order to diagonalize $H_{\mathbf{k}_e}$, we require a description of the geometry and hopping interactions φ_{ij} . Let us start with the geometry of bilayer graphene before moving onto its hopping interactions.

Bilayer graphene consists of two layers, each with two sublattices, as shown in Fig. 2. Let us subdivide the atomic index i into the layer index $l = 1, 2$, sublattice index $\alpha = \text{A, B}$, and the unit-cell index n, m . That is, $\mathbf{R}_i = \mathbf{R}_{n,m}^{l,\alpha}$, with

$$\begin{aligned} \mathbf{R}_{n,m}^{1,\text{A}} &= n\mathbf{a}_1 + m\mathbf{a}_2, \\ \mathbf{R}_{n,m}^{1,\text{B}} &= \mathbf{r}_{n,m}^{1,\text{A}} + \mathbf{C}_1, \end{aligned} \quad (\text{A4})$$

where $n, m \in \mathcal{N}$, $\mathbf{C}_1 = (\mathbf{a}_1 + \mathbf{a}_2)/3$, $\mathbf{a}_1 = a(3^{1/2}, -1, 0)/2$, $\mathbf{a}_2 = a(3^{1/2}, 1, 0)/2$. In the second layer, these vectors are rotated in plane by some angle θ and displaced by the vertical vector $\mathbf{d} = (0, 0, d)$ [46]. We use $d = 3.35 \text{ \AA}$. For $\theta = 0$, the two layers are in the AA configuration, and for $\theta = \pi/3$, the two layers are in the AB configuration.

Only certain angles create commensurate lattices which we can reasonably model. These angles are given by [46,47]

$$\cos \theta = \frac{3m_0^2 + 3m_0r + r^2/2}{3m_0^2 + 3m_0r + r^2}, \quad (\text{A5})$$

where m_0 and r are coprime positive integers. The superlattice created by twisting by this angle is defined by the superlattice vectors [47]

$$\begin{aligned} \mathbf{A}_1 &= \begin{cases} m_0\mathbf{a}_1 + (m_0 + r)\mathbf{a}_2, & r \neq 3n \\ (m_0 + r/3)\mathbf{a}_1 + (r/3)\mathbf{a}_2, & r = 3n \end{cases} \\ \mathbf{A}_2 &= \begin{cases} -(m_0 + r)\mathbf{a}_1 + (2m_0 + r)\mathbf{a}_2, & r \neq 3n \\ -(r/3)\mathbf{a}_1 + (m_0 + 2r/3)\mathbf{a}_2, & r = 3n \end{cases} \end{aligned} \quad (\text{A6})$$

where $n \in \mathcal{N}$. The number of unit cells contained within this supercell is

$$N_{uc} = \begin{cases} 3m_0^2 + 3m_0r + r^2, & r \neq 3n \\ m_0^2 + m_0r + r^2/3, & r = 3n \end{cases} \quad (\text{A7})$$

and the number of atoms contained within the supercell of size $|\mathbf{A}_i| = aN_{uc}^{1/2}/2$ is $N = 4N_{uc}$. The related Moiré period is $a/2 \sin(\theta/2)$. The Moiré period and superstructure coincide when $r = 1$, such that $r > 1$ structures correspond nearly to some $r = 1$ structure [28]. In the following discussion, we will focus on the $r = 1$ structures. For the remaining geometry of the $r > 1$ structures, see Refs. [46,47].

The twisted supercell has reciprocal lattice vectors

$$\begin{aligned} \mathbf{G}_1 &= [(2m_0 + r)\mathbf{b}_1 + (m_0 + r)\mathbf{b}_2]/N_{uc}, \\ \mathbf{G}_2 &= [-(m_0 + r)\mathbf{b}_1 + m_0\mathbf{b}_2]/N_{uc}, \end{aligned} \quad (\text{A8})$$

where $\mathbf{b}_1 = 2\pi(1/3^{1/2}, -1, 0)/a$ and $\mathbf{b}_2 = 2\pi(1/3^{1/2}, 1, 0)/a$ are the reciprocal lattice vectors of the graphene unit cell. As the supercell shares the hexagonal pattern of graphene, so too does the reciprocal lattice share the hexagonal first Brillouin zone. This BZ has two Dirac points: $\mathbf{K}_1 = (\mathbf{G}_1 + 2\mathbf{G}_2)/3$ and $\mathbf{K}_2 = (2\mathbf{G}_1 + \mathbf{G}_2)/3$ [29,47]. With the geometry established, let us describe the hopping interaction.

We divide the hopping interactions into three parts: the self-energy (φ_{ii}), the intralayer hopping (φ_{ij}^{\parallel}), and interlayer hopping (φ_{ij}^{\perp}). The self-energy is neglected in this model, as only one orbital is considered and the self-energy will only serve to shift the entire band structure by φ_{ii} . We restrict the intralayer hopping to the nearest-neighbor interactions which dominate the low-energy interactions in graphene [37]. The interlayer hopping is calculated following Refs. [28,48]. This approach screens the interaction between atoms if there is another atom lying between them. With these descriptions, we can now model the electronic behavior of bilayer graphene. As an example, consider AB-stacked graphene ($\theta = \pi/3$), where we write the following Hamiltonian matrix:

$$H_{\text{TB}} = \begin{bmatrix} -\varphi_e & -\varphi_{\parallel}g & \varphi_{\text{AB}}^{\perp}g & \varphi_{\text{BB}}^{\perp}g^* \\ -\varphi_{\parallel}g^* & -\varphi_e & \varphi_{\text{AA}}^{\perp} & \varphi_{\text{AB}}^{\perp}g \\ \varphi_{\text{AB}}^{\perp}g^* & \varphi_{\parallel} & \varphi_e & -\varphi_{\parallel}g \\ \varphi_{\text{BB}}^{\perp}g & \varphi_{\text{AB}}^{\perp}g^* & -\varphi_{\parallel}g^* & \varphi_e \end{bmatrix}, \quad (\text{A9})$$

where $g = \sum_l \exp(-i\mathbf{C}_l \cdot \mathbf{k}_e)$ is the phase factor that arises from the interaction between the Fourier transform and the vectors connecting the three nearest neighbors, \mathbf{C}_i , with

TABLE I. Tight-binding parametrization for electron and electron-phonon coupling (EPC) simulations.

Hopping	(eV)	EPC	(eV)
φ_{\parallel}	2.90	β	0.03
$\varphi_{\text{AA}}^{\perp}$	0.40	β_{AA}^*	0.00
$\varphi_{\text{AB}}^{\perp}$	2.30	β_{AB}^*	0.00
$\varphi_{\text{BB}}^{\perp}$	0.15	β_{BB}^*	0.00

$\mathbf{C}_2 = \mathbf{C}_1 - \mathbf{a}_1$ and $\mathbf{C}_3 = \mathbf{C}_1 - \mathbf{a}_2$. The parametrization used here follows Ref. [28], which reproduces (interlayer) or follows (intralayer) the established parametrization of AB-stacked bilayer graphene, as given in Table I.

APPENDIX B: ELECTRON-PHONON COUPLING

Within perturbation theory, the electron-phonon coupling between an electron in an initial state $|\mathbf{k}_e, i\rangle$ (wave number \mathbf{k}_e and band i), a final state $|\mathbf{k}_e + \mathbf{k}_p, j\rangle$, and a phonon with wave number \mathbf{k}_p and polarization α is

$$M_{e-p}^{(ij,\alpha)}(\mathbf{k}_e, \mathbf{k}_p) = \left(\frac{\hbar}{2m\omega_{\mathbf{k}_p, \alpha}} \right)^{1/2} \langle \mathbf{k}_e + \mathbf{k}_p, j | \frac{\partial H_e}{\partial \mathbf{e}_{\mathbf{k}_p, \alpha}} | \mathbf{k}_e, i \rangle, \quad (\text{B1})$$

where H_e is the electronic Hamiltonian of choice, e.g., the tight-binding Hamiltonian discussed in Appendix A or the Kohn-Sham potential within DFT, and $\mathbf{e}_{\mathbf{k}_p, \alpha}$ is the phonon eigenvector. This element can be evaluated numerically within density functional perturbation theory (DFPT) or analytically within tight-binding theory. The former is well covered by Ref. [49]. Let us examine the latter, dropping the subscript \mathbf{k}_p, α for brevity. Furthermore, let us focus on the in-plane phonons which drive phonovoltaic operation.

In Appendix A we discuss the wave functions. Here, we are primarily concerned with the central term $\partial H / \partial \mathbf{e}$. In the tight-binding model of bilayer graphene presented in Appendix A, the Hamiltonian is

$$H = - \sum_{ij} \varphi_{ij} (d_i^{\dagger} d_j + \text{H.c.}) \pm \varphi_e d_i^{\dagger} d_j \delta_{ij}, \quad (\text{B2})$$

where H.c. denotes the missing Hermitian conjugate term. While in-plane atomic motion affects the hopping interaction, it does not affect the interlayer potential. Thus, taking the derivative of this Hamiltonian with respect to \mathbf{e} gives [50]

$$\partial H / \partial \mathbf{e} = \Delta H = \sum_{ij} \frac{\partial \varphi_{ij}}{\partial a_{ij}} \frac{\mathbf{C}_{ij} \cdot \mathbf{e}_i - \mathbf{C}_{ij} \cdot \mathbf{e}_j}{a_{ij}} (d_i^{\dagger} d_j + \text{H.c.}), \quad (\text{B3})$$

where \mathbf{e}_i is the displacement of atom i due to the phonon mode, \mathbf{C}_{ij} is the vector connecting atoms i and j , and $a_{ij} = |\mathbf{C}_{ij}|$ is the magnitude of this vector.

As in Appendix A, we must Fourier transform this element into \mathbf{k}_e space in order to reduce our Hamiltonian into an $N \times N$ matrix.

The resulting electron-phonon matrix elements are [50]

$$\langle \mathbf{k}_e', n | \Delta H | \mathbf{k}_e, m \rangle = \Delta H_{n,m}(\mathbf{k}_e, \mathbf{k}_p) \frac{\partial \varphi_{nm}}{\partial a_{nm}} \frac{\mathbf{C}_{nm} \cdot \mathbf{e}_n \exp(i\mathbf{k}_e \cdot \mathbf{C}_{nm}) - \mathbf{C}_{nm} \cdot \mathbf{e}_m \exp(i\mathbf{k}_e' \cdot \mathbf{C}_{nm})}{a_{nm}}, \quad (\text{B4})$$

where $\mathbf{k}_e' = \mathbf{k}_e + \mathbf{k}_p$. As an example, consider the electron-phonon coupling matrix in AB bilayer graphene. Let

$$\begin{aligned} \mathbf{h} &= \sum_l \mathbf{C}_l \cdot \mathbf{e}_i \exp(i\mathbf{k}_e \cdot \mathbf{C}_l), \\ \zeta &= \mathbf{h}(\mathbf{k}_e) \cdot \mathbf{e}_A + \mathbf{h}(\mathbf{k}_e + \mathbf{k}_p) \cdot \mathbf{e}_B, \\ \zeta^* &= \mathbf{h}^*(\mathbf{k}_e + \mathbf{k}_p) \cdot \mathbf{e}_A + \mathbf{h}^*(\mathbf{k}_e) \cdot \mathbf{e}_B. \end{aligned} \quad (\text{B5})$$

Then, the electron-phonon coupling matrix is

$$\Delta H_{\mathbf{k}_e, \mathbf{k}_p} = \beta_{\parallel} \begin{bmatrix} 0 & \zeta & \beta_{AB}^* \zeta & \beta_{BB}^* \zeta^* \\ \zeta^* & 0 & 0 & \beta_{AB}^* \zeta \\ \beta_{AB}^* \zeta^* & 0 & 0 & \zeta \\ \beta_{BB}^* \zeta & \beta_{AB}^* \zeta^* & \zeta^* & 0 \end{bmatrix}, \quad (\text{B6})$$

where $\beta_{ij} = \partial \varphi_i / a_{ij} \partial a_{ij}$ and $\beta_{ij}^* = \beta_i / \beta_{\parallel}$.

In general, we expect that the intralayer contributions dominate their interlayer counterparts, particularly for the in-plane phonon modes considered here. Our argument is as follows: First, the interlayer hopping interactions are approximately an order of magnitude weaker than the intralayer hopping interactions. Second, the term $\mathbf{C}_{ij} \cdot \mathbf{e}_i$ significantly reduces (or prohibits) the interlayer coupling between the nearest and second-nearest neighbors, i.e., those which interact non-negligibly. For example, this term is the reason the interlayer

AA coupling element vanishes in the above electron-phonon coupling matrix.

Thus, we only require a single fitting parameter (β_{\parallel}) and the phonon and electron eigenvalues and eigenvectors in order to calculate the electron-phonon coupling element. In graphene, electrons primarily interact with two phonon modes: the Γ -point LO mode (E_{2g} , 198 meV) and the K -point TO mode (A_1' , 164 meV). Canonically, the associated graphene eigenvectors are [50,51]

$$\mathbf{e}_{\mathbf{k}_p \rightarrow 0, \text{LO}}^{(i)} = \pm \frac{1}{\sqrt{2}} \frac{\mathbf{k}_p}{|\mathbf{k}_p|}, \quad (\text{B7})$$

$$\mathbf{e}_{\mathbf{k}_p = K, \text{TO}}^{(A)} = \frac{1}{\sqrt{2}} (-i, -1, 0), \quad (\text{B8})$$

$$\mathbf{e}_{\mathbf{k}_p = K, \text{TO}}^{(B)} = \frac{1}{\sqrt{2}} (-i, 1, 0), \quad (\text{B9})$$

where i is the atomic index and the \pm refers to the A (+) and B (−) site carbon atom. In twisted bilayer graphene, the eigenvectors are rotated along with the lattice vectors in the twisted graphene layer. That is, we assume that the in-plane interactions determine the behavior of the phonon modes. Our DFPT calculations support this assumption, as these eigenvectors are identical in single-layer, AA-, and AB-stacked graphene. Finally, we take $\beta_{\parallel} = 30$ meV in order to fit our zero-field results to our DFPT results.

-
- [1] O. Madelung, *Semiconductors: Data Handbook* (Springer, Berlin, 2004).
- [2] S. Adachi, *Properties of Group-IV, III-V, and II-IV Semiconductors* (Wiley, Chichester, 2005).
- [3] W. Strehlow and E. Cook, *J. Phys. Chem. Ref. Data* **2**, 163 (1973).
- [4] X. L. Ruan and M. Kaviani, *Phys. Rev. B* **73**, 155422 (2006).
- [5] X. Ruan and M. Kaviani, *J. Heat Transfer* **129**, 3 (2007).
- [6] S. Shin, C. Melnick, and M. Kaviani, *Phys. Rev. B* **87**, 075317 (2013).
- [7] S. Shin and M. Kaviani, *Phys. Rev. B* **91**, 085301 (2015).
- [8] C. Melnick and M. Kaviani, *Phys. Rev. B* **93**, 094302 (2016).
- [9] C. Melnick and M. Kaviani, *Phys. Rev. B* **93**, 125203 (2016).
- [10] C. Melnick and M. Kaviani, *Phys. Rev. B* **94**, 245412 (2016).
- [11] J. Maultzsch, S. Reich, C. Thomsen, H. Requardt, and P. Odejón, *Phys. Rev. Lett.* **92**, 075501 (2004).
- [12] S. Piscanec, M. Lazzeri, F. Mauri, A. C. Ferrari, and J. Robertson, *Phys. Rev. Lett.* **93**, 185503 (2004).
- [13] N. Bonini, M. Lazzeri, N. Marzari, and F. Mauri, *Phys. Rev. Lett.* **99**, 176802 (2007).
- [14] A. Ferrari, *Solid State Commun.* **143**, 47 (2007).
- [15] V. Georgakilas, M. Otyepka, A. B. Bourlinos, V. Chandra, N. Kim, K. C. Kemp, P. Hobza, R. Zboril, and K. S. Kim, *Chem. Rev.* **112**, 6156 (2012).
- [16] M. Pumera and C. Hong, *Chem. Soc. Rev.* **42**, 5987 (2013).
- [17] H. Liu, Y. Liu, and D. Zhu, *J. Mater. Chem.* **21**, 3335 (2011).
- [18] M. S. Nevius, M. Conrad, F. Wang, A. Celis, M. N. Nair, A. Taleb-Ibrahimi, A. Tejada, and E. H. Conrad, *Phys. Rev. Lett.* **115**, 136802 (2015).
- [19] M. O. Goerbig, *Rev. Mod. Phys.* **83**, 1193 (2011).
- [20] K. S. Novoselov, A. K. Geim, S. V. Morozov, D. Jiang, Y. Zhang, S. V. Dubonos, I. V. Grigorieva, and A. A. Firsov, *Science* **306**, 666 (2004).
- [21] F. Schwierz, *Nat. Nanotechnol.* **5**, 487 (2010).
- [22] C. Park, J. Ryou, S. Hong, B. G. Sumpter, G. Kim, and M. Yoon, *Phys. Rev. Lett.* **115**, 015502 (2015).
- [23] Y. Zhang, T.-T. Tang, C. Girit, Z. Hao, M. Martina, A. Zettl, M. Crommie, Y. Shen, and F. Wang, *Nature (London)* **459**, 820 (2009).
- [24] F. Xia, D. B. Farmer, Y.-m. Lin, and P. Avouris, *Nano Lett.* **10**, 715 (2010).
- [25] J.-B. Liu, P.-J. Li, Y.-F. Chen, Z.-G. Wang, F. Qi, J.-R. He, B.-J. Zheng, J.-H. Zhou, W.-L. Zhang, L. Gu, and T.-R. Li, *Sci. Rep.* **5**, 15285 (2015).
- [26] E. V. Castro, K. S. Novoselov, S. V. Morozov, N. M. R. Peres, J. M. B. L. dos Santos, J. Nilsson, F. Guinea, A. K. Geim, and A. H. C. Neto, *Phys. Rev. Lett.* **99**, 216802 (2007).

- [27] P. Gava, M. Lazzeri, A. M. Saitta, and F. Mauri, *Phys. Rev. B* **79**, 165431 (2009).
- [28] A. O. Sboychakov, A. L. Rakhmanov, A. V. Rozhkov, and F. Nori, *Phys. Rev. B* **92**, 075402 (2015).
- [29] E. Mele, *Phys. Rev. B* **81**, 161405 (2010).
- [30] L. A. Gonzalez-Arraga, J. L. Lado, F. Guinea, and P. San-Jose, *Phys. Rev. Lett.* **119**, 107201 (2017).
- [31] A. Sboychakov, A. Rozhkov, A. Rakhmanov, and F. Nori, [arXiv:1707.08886](https://arxiv.org/abs/1707.08886).
- [32] Z. Yan, Z. Peng, Z. Sun, J. Yao, Y. Zhu, Z. Liu, P. M. Ajayan, and J. M. Tour, *ACS Nano* **5**, 8187 (2011).
- [33] Z. Peng, Z. Yan, Z. Sun, and J. M. Tour, *ACS Nano* **5**, 8241 (2011).
- [34] E. McCann and M. Koshino, *Rep. Prog. Phys.* **76**, 056503 (2013).
- [35] G. Painter and D. Ellis, *Phys. Rev. B* **1**, 4747 (1970).
- [36] C. J. Tabert and E. J. Nicol, *Phys. Rev. B* **86**, 075439 (2012).
- [37] A. Rozhkov, A. Sboychakov, A. Rakhmanov, and F. Nori, *Phys. Rep.* **648**, 1 (2016).
- [38] P. Giannozzi, S. Baroni, N. Bonini, M. Calandra, R. Car, C. Cavazzoni, D. Ceresoli, G. L. Chiarotti, M. Cococcioni, I. Dabo *et al.*, *J. Phys.: Condens. Matter* **21**, 395502 (2009).
- [39] N. Troullier and J. L. Martins, *Phys. Rev. B* **43**, 1993 (1991).
- [40] K. Kim, S. Coh, L. Z. Tan, W. Regan, J. M. Yuk, E. Chatterjee, M. F. Crommie, M. L. Cohen, S. G. Louie, and A. Zettl, *Phys. Rev. Lett.* **108**, 246103 (2012).
- [41] A. Jorio and L. G. Cançado, *Solid State Commun.* **175–176**, 3 (2013), Special Issue: Graphene V: Recent Advances in Studies of Graphene and Graphene analogs.
- [42] K. Kang, D. Abdula, D. G. Cahill, and M. Shim, *Phys. Rev. B* **81**, 165405 (2010).
- [43] H. Wang, J. Strait, P. George, S. Shivaraman, and V. Sheilds, *Appl. Phys. Lett.* **96**, 081917 (2010).
- [44] T. Fang, A. Konar, H. Xing, and D. Jena, *Phys. Rev. B* **84**, 125450 (2011).
- [45] J. Chauhan and J. Guo, *Appl. Phys. Lett.* **95**, 023120 (2009).
- [46] J. M. B. Lopes dos Santos, N. M. R. Peres, and A. H. Castro Neto, *Phys. Rev. Lett.* **99**, 256802 (2007).
- [47] J. M. B. Lopes dos Santos, N. M. R. Peres, and A. H. Castro Neto, *Phys. Rev. B* **86**, 155449 (2012).
- [48] M. S. Tang, C. Z. Wang, C. T. Chan, and K. M. Ho, *Phys. Rev. B* **53**, 979 (1996).
- [49] N. Vast and S. Baroni, *Phys. Rev. B* **61**, 9387 (2000).
- [50] T. Sohler, M. Calandra, C.-H. Park, N. Bonini, N. Marzari, and F. Mauri, *Phys. Rev. B* **90**, 125414 (2014).
- [51] J. L. Mañes, *Phys. Rev. B* **76**, 045430 (2007).